J. Fluid Mech. (2024), *vol*. 987, A15, doi:10.1017/jfm.2024.385

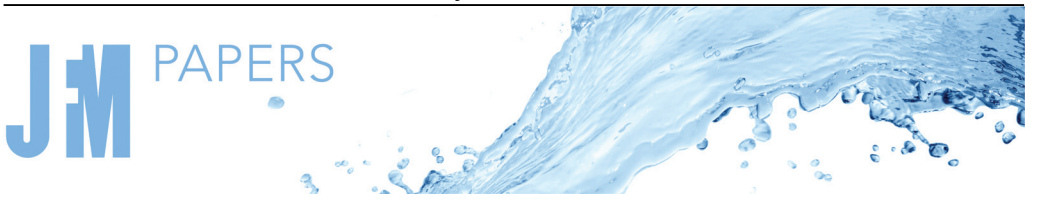

Role of volatility and thermal properties in droplet spreading: a generalisation to Tanner's law

Zhenying Wang[1,2,†], **George Karapetsas**[3], **Prashant Valluri**[4] **and Chihiro Inoue**[1]

[1]Department of Aeronautics and Astronautics, Kyushu University, Nishi-Ku, Motooka 744, Fukuoka 819-0395, Japan

[2]International Institute for Carbon-Neutral Energy Research (WPI-I^{2}CNER), Kyushu University, Nishi-Ku, Motooka 744, Fukuoka 819-0395, Japan

[3]Department of Chemical Engineering, Aristotle University of Thessaloniki, Thessaloniki 54124, Greece

[4]Institute of Multiscale Thermofluids, School of Engineering, University of Edinburgh, Edinburgh EH9 3JL, UK

(Received 4 August 2023; revised 11 April 2024; accepted 15 April 2024)

Droplet spreading is ubiquitous and plays a significant role in liquid-based energy systems, thermal management devices and microfluidics. While the spreading of non-volatile droplets is quantitatively understood, the spreading and flow transition in volatile droplets remains elusive due to the complexity added by interfacial phase change and non-equilibrium thermal transport. Here we show, using both mathematical modelling and experiments, that the wetting dynamics of volatile droplets can be scaled by the spatial–temporal interplay between capillary, evaporation and thermal Marangoni effects. We elucidate and quantify these complex interactions using phase diagrams based on systematic theoretical and experimental investigations. A spreading law of evaporative droplets is derived by extending Tanner's law (valid for non-volatile liquids) to a full range of liquids with saturation vapour pressure spanning from 10^1 to 10^4 Pa and on substrates with thermal conductivity from 10^{-1} to 10^3 W m^{-1} K^{-1}. In addition to its importance in fluid-based industries, the conclusions also enable a unifying explanation to a series of individual works including the criterion of flow reversal and the state of dynamic wetting, making it possible to control liquid transport in diverse application scenarios.

Key words: drops, contact lines, thermocapillarity

† Email address for correspondence: zhenying.wang@aero.kyushu-u.ac.jp

1. Introduction

Wetting presents the basic state when a finite volume of liquid contacts a solid substrate (De Gennes 1985; Bonn *et al.* 2009). The requirement for wetting differs for different applications and, hence, the design principles. For example, good wetting enables efficient liquid supply and avoids drying out in phase change thermal management, e.g. electronics cooling (Mudawar 2001). In condensation, a quick wetting transition will increase the substrate's thermal resistance and worsen the condensation performance (Rose 2002). A full understanding of the interplay between wetting and phase change is thus necessary for on-demand design of various energy systems (Wang, Zhang & Li 2017; Breitenbach, Roisman & Tropea 2018; Tu *et al.* 2018) and in other microfluids-based industries (Teh *et al.* 2008; Zheng *et al.* 2010; Chen *et al.* 2022; Cheng *et al.* 2024).

The wetting dynamics of non-volatile liquids are known to be governed by capillary force and viscous dissipation. Specifically, the spreading rate of a non-volatile Newtonian droplet in perfect wetting cases can be quantitatively described by Tanner's law, $R(t) \sim t^{1/10}$ (Tanner 1979; Lelah & Marmur 1981; Blake 2006), which can be derived mathematically by employing the lubrication approximation and balancing the effect of capillary forces with the resisting viscous forces generated by the droplet motion (Voinov 1976; Carlson 2018; Pang & Náraigh 2022). The spreading law has then been validated by successive experiments (Marmur 1983) and further extended to non-Newtonian liquids (Rafaï, Bonn & Boudaoud 2004; Jalaal, Stoeber & Balmforth 2021), gravity-influenced cases (Cazabat & Stuart 1986), near-critical cases (Saiseau *et al.* 2022), liquids on non-rigid solids and on thin liquid films (Carré, Gastel & Shanahan 1996; Cormier *et al.* 2012), as well as under-liquid systems (Goossens *et al.* 2011; Mitra & Mitra 2016).

Compared with non-volatile liquids, the spreading of volatile liquids is more complex and remains elusive owing to the complexity added by interfacial phase change and non-equilibrium thermal transport (Berteloot *et al.* 2008; Jambon-Puillet *et al.* 2018; Wang *et al.* 2019, 2020, 2022). Specifically, the non-uniform mass flux tends to recede the liquid–air interface especially near the three phase contact line. The effect of evaporation cooling and the non-uniform pathway for heat dissipation induce temperature gradient and therefore thermal Marangoni flow, which complex the flow pattern inside the droplet and further affect the spreading dynamics.

A full elucidation of these interacting mechanisms requires a quantitative description of each physical process, as well as a thorough understanding of all influencing parameters. In this research, we combine experimental and numerical approaches to address these issues and revisit the theoretical descriptions of flow interaction in liquid spreading. The explorations enable us to quantify the strength of dominating physics that varies spatially and temporally, which on the other hand provides a unifying criterion for flow reversal (Hu & Larson 2005; Ristenpart *et al.* 2007; Xu & Luo 2007; Xu, Luo & Guo 2010), pattern formation (Deegan *et al.* 1997; Hu & Larson 2006; Li *et al.* 2015) and Marangoni–capillary interactions (Tsoumpas *et al.* 2015; Shiri *et al.* 2021; Yang *et al.* 2022) in drying droplets.

Specifically, we investigate the flow state and the resulting wetting dynamics of volatile liquids on thermal conductive substrates. In the numerical aspect, previous lubrication-type models usually consider boundary conditions with uniform heating (Anderson & Davis 1995; Ajaev 2005) or preset substrate temperature/temperature gradient (Karapetsas, Sahu & Matar 2013; Dai *et al.* 2016; Charitatos & Kumar 2020; Wang *et al.* 2021), which failed to illustrate the non-negligible role of non-isothermal heat conduction in the overall process. In addition, the numerical and experimental investigations have at large been developing in parallel without strict comparisons that consider the specific application scenarios. In this work we take account of the mass,

momentum and energy transport in the liquid phase, as well as the heat conduction through the solid substrate. We apply the assumption of a precursor film (ultrathin adsorbed liquid layer; Kavehpour, Ovryn & McKinley 2003; Ajaev 2005; Hoang & Kavehpour 2011) existing in front of the three-phase contact line, which eliminates the stress singularity and avoids experimental fitting of contact line motion, e.g. preset advancing/receding contact angles or a finite slip. A strict one-to-one comparison is then conducted between experimental and numerical results for a broad range of liquid–solid combinations. The reliability of the theoretical models further give rise to a general principle of flow transition and spreading rate of volatile droplets.

The rest of this paper is organised as follows. In § 2, we introduce the formulated mathematical model, the scaling and simplification and the numerical method. Section 3 introduces the material preparation, the detailed experimental set-up and procedures. Section 4 presents the numerical and experimental results including the dominating mechanisms, the transition of flow pattern and their relations to the spreading dynamics. Section 5 summarises the key findings of this work, and shares our perspectives on liquid spreading with/without interfacial phase change.

2. Formulation of the numerical model

We consider a thin liquid droplet (Newtonian fluid, with aspect ratio $\varepsilon = \hat{H}_0/\hat{R}_0 \ll 1$, where $\hat{H}_0$ is the initial droplet height, $\hat{R}_0$ is the initial droplet contact radius) sitting on a thermal conductive solid substrate with finite thickness and surrounded by a mixture of its own vapour and non-condensing gas, e.g. a water droplet in humid air, as indicated by figure 1(*a*). The low aspect ratio allows for the application of lubrication theory which simplifies the Navier–Stokes equations, while capturing the dominating physical processes. The lubrication approximation is valid for droplets with small and moderate contact angles typically less than 40°, which is the case of current research on complete wetting and partial wetting scenarios. A precursor film is assumed to exist at the solid surface in front of the three phase contact line. This avoids the stress singularity that may arise due to the inherent contradiction in simultaneously assuming the no-slip boundary condition and expecting a displacement between liquid and solid with contact line motion.

2.1. *Governing equations*

A cylindrical coordinate system, $(\hat{r}, \theta, \hat{z})$, is applied to solve the velocity field, $\hat{\boldsymbol{u}} = (\hat{u}, \hat{v}, \hat{w})$, where $\hat{u}$, $\hat{v}$ and $\hat{w}$ correspond to the horizontal, azimuthal and vertical components of the velocity field, respectively. The liquid–vapour interface locates at $\hat{z} = \hat{h}(\hat{r}, \hat{t})$ and the liquid–solid at $\hat{z} = 0$. The liquid phase is governed by the continuity, momentum and energy equations (figure 1(*b*)),

$$\hat{\boldsymbol{\nabla}} \cdot \hat{\boldsymbol{u}} = 0, \tag{2.1}$$

$$\hat{\rho}\left(\frac{\partial \hat{\boldsymbol{u}}}{\partial \hat{t}} + \hat{\boldsymbol{u}} \cdot \hat{\boldsymbol{\nabla}}\hat{\boldsymbol{u}}\right) = \hat{\boldsymbol{\nabla}} \cdot \hat{\boldsymbol{E}}, \tag{2.2}$$

$$\hat{\rho}\hat{c}_p\left(\frac{\partial \hat{T}}{\partial \hat{t}} + \hat{\boldsymbol{u}} \cdot \hat{\boldsymbol{\nabla}}\hat{T}\right) = \hat{\boldsymbol{\nabla}} \cdot (\hat{k}\hat{\boldsymbol{\nabla}}\hat{T}), \tag{2.3}$$

where liquid density $\hat{\rho}$, specific heat capacity $\hat{c}_p$ and thermal conductivity $\hat{k}$ are set as constant, $\hat{T}$ denotes temperature, $\hat{t}$ denotes time and $\hat{\boldsymbol{E}}$ denotes the total stress tensor at the

liquid side,

$$\hat{\boldsymbol{E}} = -\hat{p}\boldsymbol{I} + \hat{\mu}(\hat{\boldsymbol{\nabla}}\hat{\boldsymbol{u}} + \hat{\boldsymbol{\nabla}}\hat{\boldsymbol{u}}^{\mathrm{T}}), \tag{2.4}$$

where $\hat{p}$ is the pressure of the liquid phase, $\hat{\mu}$ is the dynamic viscosity of the liquid and is set as constant and $\boldsymbol{I}$ is the identity tensor.

At the liquid–gas interface, the liquid velocity and geometry satisfy a force balance both in the normal and tangential directions (figure 1(*b*)). The normal stress balance relates the pressure difference, surface tension, mean curvature and van der Waals interactions,

$$-\hat{p} + \boldsymbol{n}\cdot\hat{\boldsymbol{\tau}}\cdot\boldsymbol{n} = 2\hat{\kappa}\hat{\sigma} + \hat{\Pi} - \hat{p}_g, \tag{2.5}$$

where $\hat{p}_g$ is the total pressure of the gas phase, $\hat{\sigma}$ is the liquid–gas surface tension, $\hat{\boldsymbol{\tau}}$ is the extra stress tensor of the liquid phase. $2\hat{\kappa} = -\hat{\boldsymbol{\nabla}}_S\cdot\boldsymbol{n}$ is twice the mean curvature of the free surface, $\hat{\boldsymbol{\nabla}}_S = (\boldsymbol{I} - \boldsymbol{nn})\cdot\hat{\boldsymbol{\nabla}}$ is the surface gradient operator. Here $\hat{\Pi}$ denotes the disjoining pressure between interfaces that accounts for intermolecular interactions (De Gennes, Hua & Levinson 1990),

$$\hat{\Pi} = \frac{\hat{A}}{6\pi\hat{h}^3}, \tag{2.6}$$

with $\hat{A}$ being the dimensional Hamaker constant, $\hat{h}$ being the location of the liquid–gas interface.

The tangential stress balance relates the shear stress and the surface tension gradient. By ignoring the shear stress from the gas phase due to small viscosity, we arrive at

$$\boldsymbol{n}\cdot\hat{\boldsymbol{E}}\cdot\boldsymbol{t} = \hat{\boldsymbol{\nabla}}_S\hat{\sigma}\cdot\boldsymbol{t}, \tag{2.7}$$

where $\boldsymbol{t}$ refers to the outward vector which is tangential to the interface.

The motion of the liquid–gas interface (free surface) can be described with the kinematic boundary condition, expressed as

$$\frac{\partial\hat{h}}{\partial\hat{t}} + \hat{u}_S\frac{\partial\hat{h}}{\partial\hat{r}} + \frac{\hat{v}_S}{\hat{r}}\frac{\partial\hat{h}}{\partial\theta} = \hat{w}_S. \tag{2.8}$$

The boundary equation of mass balance (liquid–gas) can be expressed by the relationship between the velocity of the liquid solution, $\hat{\boldsymbol{u}}$, the velocity of the liquid–gas interface, $\hat{\boldsymbol{u}}_S = (\hat{u}_S, \hat{v}_S, \hat{w}_S)$, and the interfacial mass flux, $\hat{J}$:

$$(\hat{\boldsymbol{u}} - \hat{\boldsymbol{u}}_S)\cdot n = \frac{\hat{J}}{\hat{\rho}}, \tag{2.9}$$

where $\hat{J}$ denotes the interfacial mass flux of evaporating liquid. The jump energy balance can then be derived accounting for the heat release at the liquid–vapour interface and ignoring the heat conduction into the gas phase. This assumption is reasonable in cases where $\hat{k}_{air} \ll \hat{k}$:

$$\hat{J}\hat{L} + \hat{k}\hat{\boldsymbol{\nabla}}\hat{T}\cdot\boldsymbol{n} = 0, \tag{2.10}$$

where $\hat{L}$ denotes the latent heat of vapourisation.

The Hertz–Knudsen equation is commonly used for predicting the mass flux induced by evaporation or condensation towards a liquid–vapour interface. The following relation can be derived combining the Hertz–Knudsen equation (Plesset & Prosperetti 1976; Moosman

& Homsy 1980), the chemical potential difference across the liquid–gas interface (Atkins, Atkins & de Paula 2014), and the ideal gas assumption,

$$\hat{J} = \hat{p}_{v,sat}\sqrt{\frac{\hat{M}}{2\pi\hat{R}_g\hat{T}_g}}\left(\frac{\hat{M}}{\hat{\rho}\hat{R}_g\hat{T}_g}(\hat{p}-\hat{p}_g)+\frac{\hat{M}\hat{L}}{\hat{R}_g\hat{T}_g^2}(\hat{T}_S-\hat{T}_g)+\ln\left(\frac{1}{\chi_{vapour}}\right)\right), \tag{2.11}$$

where $\hat{p}_{v,sat}$ is the saturation vapour pressure, $\hat{M}$ is the molar mass of the liquid, $\hat{R}_g$ is the gas constant, $\hat{T}_g$ is the temperature of gas phase, $\hat{T}_S$ is the temperature at the liquid–gas interface and χ_{vapour} is the relative vapour concentration, i.e. ratio of partial vapour pressure to saturation vapour pressure in the gas phase.

2.2. *Scaling*

The key parameters are scaled as follows:

$$\left.\begin{gathered}\hat{r}=\hat{R}_0 r,\quad \hat{z}=\hat{H}_0 z,\quad (\hat{u},\hat{w})=\left(\hat{u}^*u,\frac{\hat{H}_0}{\hat{R}_0}\hat{u}^*w\right),\\ \hat{T}=\hat{T}_{ref}+T\Delta\hat{T},\quad \hat{\sigma}=\hat{\sigma}_0\sigma=\hat{\sigma}_0\left(1+\frac{\hat{\eta}_\sigma\Delta\hat{T}}{\hat{\sigma}_0}T\right),\\ \hat{t}=\frac{\hat{R}_0}{\hat{u}^*}t,\quad \hat{p}=\hat{p}_g+\frac{\hat{\mu}\hat{u}^*\hat{R}_0}{\hat{H}_0^2}p,\quad \hat{J}=\frac{\hat{k}\Delta\hat{T}}{\hat{H}_0\hat{L}}J,\end{gathered}\right\} \tag{2.12}$$

where the characteristic velocity is defined as $\hat{u}^*=\varepsilon\hat{\eta}_\sigma\Delta\hat{T}/\hat{\mu}$, $\hat{\sigma}_0$ is the liquid–gas surface tension at reference temperature, $\hat{\eta}_\sigma$ is the coefficient of surface tension to temperature, $\hat{T}_{ref}$ is the reference temperature and $\Delta\hat{T}$ is the maximum temperature difference across the droplet. The dimensionless group is thereafter derived, including the Reynolds number $Re=\hat{\rho}\hat{u}^*\hat{H}_0/\hat{\mu}$ (ratio of inertia to viscous effect), Prandtl number $Pr=\hat{\mu}\hat{c}_p/\hat{k}$ (ratio of momentum diffusivity to thermal diffusivity), evaporation number $E=\hat{k}\hat{R}_0\Delta\hat{T}/\hat{\rho}\hat{L}\hat{H}_0^2\hat{u}^*$ (measure of evaporation strength), Marangoni number $Ma=\hat{\mu}\hat{u}^*/\varepsilon\hat{\sigma}_0=\hat{\eta}_\sigma\Delta\hat{T}/\hat{\sigma}_0$ (measure of the strength of Marangoni flow), Hamaker constant $\mathcal{A}=\hat{\mathcal{A}}/6\pi\hat{\mu}\hat{u}^*\hat{R}_0\hat{H}_0$, the coefficients in the expression of mass flux $\delta=\hat{M}\hat{\eta}_\sigma\Delta\hat{T}/\hat{\rho}\hat{R}_g\hat{T}_g\hat{H}_0$ (measure of Kelvin effect), $\psi=\hat{M}\hat{L}\Delta\hat{T}/\hat{R}_g\hat{T}_g^2$ (effect of local temperature difference on the mass flux) and Jakob number $Ja=(\hat{k}\Delta\hat{T}/\hat{H}_0\hat{L}\hat{p}_{v,sat})\sqrt{2\pi\hat{R}_g\hat{T}_g/\hat{M}}$ (measuring the joint thermal effects at the interface by evaporation cooling and heat dissipation into the liquid).

For sessile droplets with slow interfacial phase change, the inertia effect can be neglected with very small Reynolds number (usually $Re<10^{-1}$ for droplet wetting and evaporation), therefore we set the Reynolds number to zero in the formulation. By further ignoring the parameter variation in the azimuthal direction, we arrive at the dimensionless governing equations, including mass conservation (2.13), momentum equation (2.14), energy equation (2.15), as well as the dimensionless boundary equations, including the normal and tangential stress boundary balance (2.16), the kinematic boundary condition (2.17), the jump energy balance (2.18) and the expression of interfacial mass flux (2.19)

(figure 1(*b*)):

$$\frac{1}{r}\frac{\partial (ru)}{\partial r} + \frac{\partial w}{\partial z} = 0, \tag{2.13}$$

$$\frac{\partial p}{\partial r} = \frac{\partial}{\partial z}\left(\frac{\partial u}{\partial z}\right), \tag{2.14}$$

$$\frac{\partial}{\partial z}\left(\frac{\partial T}{\partial z}\right) = 0, \tag{2.15}$$

$$p = -\frac{\varepsilon^2 \sigma}{Ma}\left(\frac{1}{r}\frac{\partial}{\partial r}\left(r\frac{\partial h}{\partial r}\right)\right) - \frac{\mathcal{A}}{h^3}, \quad \tau_{zr} = \frac{1}{Ma}\frac{\partial \sigma}{\partial r}, \tag{2.16}$$

$$\frac{\partial h}{\partial t} + u\frac{\partial h}{\partial r} - w + EJ = 0, \tag{2.17}$$

$$J + \frac{\partial T}{\partial z} = 0, \tag{2.18}$$

$$JaJ = \delta p + \psi (T_i - T_g) + \ln\left(\frac{1}{\chi_{vapour}}\right). \tag{2.19}$$

The above equations are integrated over the vertical direction, with the integration of velocity and temperature expressed as $f = \int_0^h u\,\mathrm{d}z$, $\Theta = \int_0^h T\,\mathrm{d}z$. The integral form of equations are subsequently discretised using a finite-element/Galerkin method; the variables are approximated using quadratic Lagrangian basis functions Φ_i. After applying the divergence theorem, we arrive at the weak form of five governing equations with five independent variables, h, p, f, Θ and J:

$$\int \left(\frac{\partial h}{\partial t}\Phi_i + EJ\Phi_i - f\frac{\partial \Phi_i}{\partial r}\right) r\,\mathrm{d}r + (rf\Phi_i)_{r=0}^{r=r_\infty} = 0, \tag{2.20}$$

$$\int \left(h\frac{\partial p}{\partial r} - \left(\frac{\partial u}{\partial z}\right)_0^h\right)\Phi_i r\,\mathrm{d}r = 0, \tag{2.21}$$

$$R = \int \left(\frac{\partial T}{\partial z}\right)_0^h \Phi_i r\,\mathrm{d}r = 0, \tag{2.22}$$

$$\int \left(\left(p + \frac{\mathcal{A}}{h^3}\right)\frac{Ma}{\varepsilon^2\sigma}\Phi_i - \frac{\partial h}{\partial r}\frac{\partial \Phi_i}{\partial r}\right) r\,\mathrm{d}r + \left(r\frac{\partial h}{\partial r}\Phi_i\right)_{r=0}^{r=r_\infty} = 0, \tag{2.23}$$

$$\int \left(JaJ - \delta p - \psi (T|_{z=h} - T_g) + \ln \chi_{vapour}\right)\Phi_i r\,\mathrm{d}r = 0. \tag{2.24}$$

Finally, we consider an Ansatz distribution function of liquid temperature T and velocity u in z axis to complete the mathematical formulation. We fit the flow velocity and the temperature distribution with a parabolic expression, i.e. $y = c_3 + c_2 z + c_1 z^2$, then derive their expressions by applying the boundary conditions at $z = 0$ and $z = h$.

At the liquid–gas interface, $z = h$, the flow velocity meets the tangential stress balance (2.16), which relates the surface tension gradient to the shear stress (multiplication of dynamic viscosity and velocity gradient). At the liquid–solid interface, $z = 0$, a no slip

boundary condition applies. The flow velocity is thereafter derived as

$$u = \left(\frac{3f}{h^2} - \frac{1}{2Ma}\frac{\partial \sigma}{\partial r}\right) z + \left(\frac{3}{4hMa}\frac{\partial \sigma}{\partial r} - \frac{3f}{2h^3}\right) z^2. \tag{2.25}$$

For the temperature distribution, the temperature meets the jump energy balance at the droplet surface, $z = h$, (2.18), which relates the temperature gradient at the liquid side to the interfacial heat flux due to phase change. At the liquid–solid interface, we consider (1) substrates with constant temperature and (2) thermal conductive substrates with finite thickness. For case (1) with constant substrate temperature, the temperature distribution in the liquid phase can be derived as

$$T = T_W + \left(\frac{3\Theta}{h^2} - \frac{3T_W}{h} + \frac{J}{2}\right) z + \left(\frac{3T_W}{2h^2} - \frac{3\Theta}{2h^3} - \frac{3J}{4h}\right) z^2. \tag{2.26}$$

For case (2) thermal conductive substrates with finite thickness $\hat{H}_{solid}$ and thermal conductivity $\hat{k}_{solid}$, the process can be simplified into a quasi-steady one-dimensional problem. Similar approximations were also adopted in research by Ristenpart *et al.* (2007), Xu *et al.* (2010) and Dunn *et al.* (2009). The boundary condition at $z = 0$ in this situation can be described as:

$$\frac{\partial T}{\partial z} = \frac{T - T_W}{Bi}, \tag{2.27}$$

where Biot number, $Bi = \hat{H}_{solid}\hat{k}/\hat{H}_0\hat{k}_{solid}$, denotes the ratio of thermal resistance of the solid phase to that of the liquid phase.

Combining the parabolic expression of temperature distribution and the boundary conditions at the liquid–solid interface and the liquid–gas interface, the distribution of liquid temperature in case (2) is thereafter derived as

$$\left.\begin{aligned} T &= c_3 + c_2 z + c_1 z^2, \\ &\text{where} \\ c_1 &= \frac{1}{3Bi + h}\left(-\frac{3BiJ}{2h} - \frac{3J}{4} - \frac{3\Theta}{2h^2} + \frac{3T_W}{2h}\right), \\ c_2 &= \frac{1}{3Bi + h}\left(\frac{hJ}{2} + \frac{3\Theta}{h} - 3T_W\right), \\ c_3 &= \frac{1}{3Bi + h}\left(\frac{BihJ}{2} + \frac{3Bi\Theta}{h} + hT_W\right). \end{aligned}\right\} \tag{2.28}$$

2.3. *Initial and boundary conditions*

In the region of $0 \le r \le 1$, the initial conditions, $t = 0$, are set as

$$h(r, 0) = h_\infty + 1 - r^2, \quad f(r, 0) = 0, \quad \Theta(r, 0) = h(r, 0)T_W, \tag{2.29a–c}$$

where h_∞ is the thickness of the precursor film and T_W is the initial temperature of the solid substrate. For zero mass flux at the precursor film region, the initial value of h_∞ is set as $\sqrt[3]{\mathcal{A}\delta/(\psi(T_W - T_g) - \ln(\chi_{vapour}))}$ by combining (2.19) ($J = 0$) and (2.16), where the disjoining pressure from intermolecular interaction prevents further evaporation of the

liquid film. The parameters at the droplet centre, $r = 0$, satisfy the symmetric boundary conditions, expressed as

$$\frac{\partial h}{\partial r}(0, t) = 0, \quad f(0, t) = 0, \quad \frac{\partial \Theta}{\partial r}(0, t) = 0. \tag{2.30a–c}$$

In the region of precursor film, $r > 1$, the parameters are set as

$$h(r, 0) = h_\infty, \quad f(r, 0) = 0, \quad \Theta(r, 0) = h_\infty T_W. \tag{2.31a–c}$$

We apply Galerkin finite-element method to solve the system of partial differential equations (PDEs). A one-dimensional mesh is constructed along the r-direction, and the length of the computational domain is set as twice the maximal spreading radius within the computational time to ensure the free development of the droplet morphology. The domain is discretised along r from 0 to r_∞ into equally spaced nodes, the total number being N_{tot}, and the density is set as 200 per dimensionless length with grid independence test of the solution. At each time step, we apply the Newton–Raphson method to obtain the solution across the computational domain progressively. The solution evolves forwards with an adaptive time interval which adjusts according to the maximum residual errors of the governing equations from the previous time step (adaptive implicit Euler method). The iterative program is written in Fortran, making use of the linear algebra package LAPACK.

3. Experimental method

As shown in figure 2, experiments are conducted with high-speed imaging and microPIV in an air-conditioned lab space with constant temperature and humidity (20 °C, 50 ± 5 %RH). We use high-speed camera (Photron FASTCAM Mini AX200 type with frame rate of 3000 fps) to trace the fast spreading of droplet upon its contact with a solid surface. To minimise the impinging force of the droplet, we set the distance between the syringe and the substrate to a similar value with the initial diameter of the spherical droplet ($V_0 = 3 \pm 0.2$ µl for 1-butanol and 2-propanol, and 0.6 ± 0.05 µl for FC-72), so that the droplet can touch the solid surface right after its generation from the syringe tip. A commercial cool plate based on Peltier module and digital PID controller (0–105 °C, ±0.2 °C) is utilised as the substrate holder which keeps the downward side substrate temperature constant.

We select 1-butanol, 2-propanol (IPA) and FC-72 as the working fluids, each with one order of magnitude larger saturation vapour pressure (table 1). Three types of solid materials are utilised, i.e. copper, SUS430 and glass, each with one order of magnitude smaller thermal conductivity. We also use copper substrates of thickness 0.3, 1.0 and 3.0 mm to demonstrate the effect of substrate thickness. The three types of substrates exhibit a highly wetting state for 1-butanol, 2-propanol and FC-72 which matches the requirement of low contact angle (less than 40°) for lubrication approximation. For each condition, we repeated the experiments at least five times. The average values of the spreading rates along with standard deviations are derived for comparison with the numerical predictions (table 4). The key thermophysical properties of different liquids and solids are given in tables 1 and 2.

To remove any oxide residuals and ensure the uniformity and smoothness of the solid surface, we fabricate substrate surfaces with mirror finishing. The surface roughness of glass, SUS430 and copper is characterised to be $Sa_{glass} = 0.258$ µm, $Sa_{SUS430} = 0.134$ µm, $Sa_{copper} = 0.291$ µm with a 3-D laser scanning microscope (OLYMPUS/LEXT OLS4000). Before each set of experiments, we prepare the solid substrate by 15 min

https://doi.org/10.1017/jfm.2024.385 Published online by Cambridge University Press

Liquid	$\hat{\rho}$ (kg m^{-3})	$\hat{\mu}$ (mPa s)	$\hat{\sigma}$ (mN m^{-1})	$\hat{\eta_\sigma}$ (mN m^{-1} K^{-1})	$\hat{k}$ (W m^{-1} K^{-1})	$\hat{c}_p$ (J kg^{-1} K^{-1})	$\hat{p}_{sat}$ (Pa)	$\hat{L}$ (kJ kg^{-1})
Water	998	1.005	72.75	−0.15	0.60	4180	2341	2257
1-butanol	810	2.573	24.57	−0.07	0.1553	2386	580	584
2-propanol	786	2.012	23.0	−0.09	0.135	1527	4420	663
FC-72	1680	0.64	10	—	0.057	1100	30 900	88
Methanol	792	0.59	22.7	−0.0773	0.204	2460	10 300	1191
Ethanol	789	1.144	22	−0.0832	0.166	2570	5786	1030
Chloroform	1490	0.563	27.5	−0.1295	0.13	957	25 900	248
Heptane	684	0.389	20.2	−0.098	0.128	2220	4621	3553
Hexane	659	0.301	18.4	−0.1022	0.125	2243	19 140	382

Table 1. Thermophysical properties of representative liquids at 293 K except FC-72 (298 K). 1-butanol, 2-propanol and FC-72 were utilised in present experiments. Water, 2-propanol, methanol, ethanol and chloroform were utilised in previous studies on circulation reversal (Ristenpart *et al.* 2007; Xu *et al.* 2010; Li *et al.* 2015) as marked in figure 5. Alkanes (e.g. heptane and hexane) were utilised in the study of Shiri *et al.* (2021) on the influence of thermal Marangoni flow on droplet geometry as marked in figure 7.

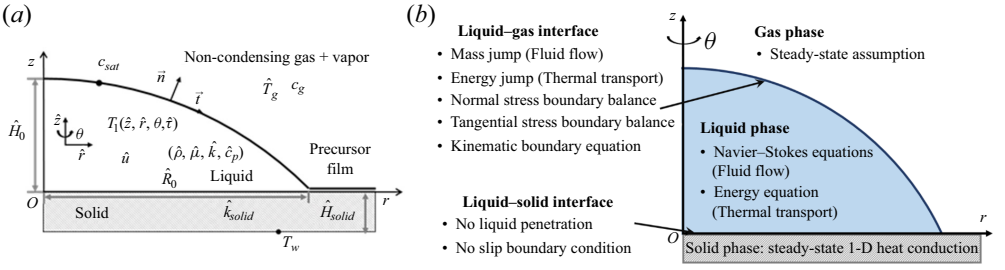

Figure 1. (*a*) A single component droplet with small aspect ratio, $\hat{H}_0/\hat{R}_0$, sitting on a solid substrate surrounded by its own vapour and non-condensing gas. Here c_{sat} denotes the saturation vapour concentration. We use $\hat{T}_g$ and c_g to denote the temperature and vapour concentration of the gas phase, which remain constant. Here $\hat{\rho}$ is the liquid density, $\hat{\mu}$ is the liquid viscosity, $\hat{k}$ is the thermal conductivity of the liquid, $\hat{c_p}$ is the specific heat capacity of the liquid, $\hat{H}_{solid}$ is the thickness of the substrate, $\hat{k}_{solid}$ is the thermal conductivity of the substrate, T_w is the temperature at the downward side of the substrate and $\vec{n}$ and $\vec{t}$ are the outward units vectors acting in normal and tangential directions to the interface. The centre of droplet base, O, is defined as the origin of the coordinate. (*b*) Governing equations that are considered in the gas, liquid and solid phases, along with the boundary equations at the central axis, the liquid–gas interface and the liquid–solid interface.

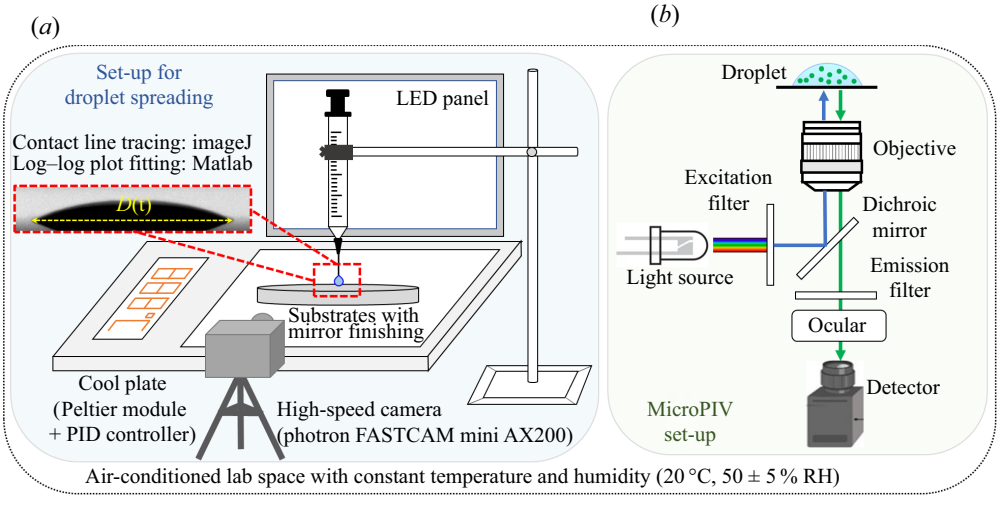

Figure 2. Experimental set-up for (*a*) droplet spreading and (*b*) microPIV visualisation of flow field inside the droplet.

ultrasonic bath with 99.8 % ethanol, then flush with large quantity of deionised water, and dry the surface with high-speed clean air flow. We start the high-speed camera immediately before the deposition of the droplet and stop recording as the droplet fully spreads.

For enhancing the image contrast, an LED light sheet panel is utilised for making clear droplet shadow. The videos are further processed with imageJ (Schneider, Rasband & Eliceiri 2012) and Matlab for extracting the evolution of contact radius and linearly fitting the log–log plot. To avoid the inertia effect of the depositing droplet (Ding & Spelt 2007; Bird, Mandre & Stone 2008; Chen, Bonaccurso & Shanahan 2013), the plot fitting focuses on inertia-free flow state regime after the droplet fully detaches from the syringe with continuous contact line advancing.

Material Type	Copper	SUS430	Glass	PDMS
k_{solid} (W m^{-1} K^{-1})	385	25	1.2	0.23

Table 2. Thermal conductivity of representative substrate materials. Copper, SUS430 and glass were utilised in present study. Glass was utilised in the work of Xu *et al.* (2010) and Hu & Larson (2006). Polydimethylsiloxane (PDMS) was utilised in the work of Ristenpart *et al.* (2007).

Microparticle image velocimetry (μPIV) is implemented to measure the flow field near the bottom of an evaporating droplet (figure 2*b*). The measurements are based on an inverted fluorescent microscope (Nikon Ts2-FL). Specifically, a green laser (468 nm) is utilised to excite the fluorescent microtracers (Fluoro-Max; green fluorescent polymer microspheres: excitation/emission 468/508 nm, diameter 1.0 μm). A CCD camera (STC-MCS510U3V) connected to the microlens captures the fluorescent signal emitted by the tracer particles. We use butanol and IPA as the test fluids, which have similar surface tension but different volatility (table 1). Experiments are conducted on slide glass for microscope with thickness of 1.1 ± 0.2 mm. The droplet size for microPIV experiments is set as 0.5 ± 0.002 μl, and is focused with 20× lens from the bottom. Each set of experiments is repeated for more than five times. The representative videos are presented in Supplementary movie 3 available at https://doi.org/10.1017/jfm.2024.385, where the video of butanol is speeded up by 20 times and the video of IPA is slowed down by 3 times with ImageJ.

4. Results and discussion

4.1. *Transition of flow states: physical mechanisms*

Figure 3 shows the evolution of flow field in a representative case, which can be characterised into three stages. At the initial stage (①) when a liquid droplet contacts a solid surface, the capillary effect drives a continuous outward flow, leading to rapid droplet spreading. In the second stage (②), the evaporation cooling effect and the non-uniform heat dissipation result in temperature gradient across the droplet surface, and induce thermal Marangoni flow from the droplet edge towards the apex. The opposing thermal Marangoni and capillary forces lead to the formation of two stagnation points (SPs) at the droplet surface. The upper SP moves towards the droplet apex as the Marangoni flow gets stronger and disappears as a recirculation vortex engulfs the whole droplet. The lower SP remains near the contact line (③) as a result of capillary–Marangoni interaction (Ristenpart *et al.* 2007; Xu & Luo 2007; Wang & Harris 2018; Wang *et al.* 2024).

Yet two questions arise as our analysis goes on. One is 'Does the SP universally exist?' and another is 'Does thermal Marangoni flow always play a role in wetting dynamics?'. These two questions are intricately related as the relative strength of thermal Marangoni flow and capillary flow decides the flow state and the formation of the SP, and therefore the wetting dynamics.

To elucidate this, we conducted detailed parametric analyses on varying combinations of liquids and solids that span five orders of magnitudes in their saturation vapour pressure and thermal conductivity. Two dominant dimensionless numbers (derived in the scaling process) are concluded to govern the interacting physics, namely, the Jakob number, *Ja*, which evaluates the balance between interfacial phase change and heat transfer into the

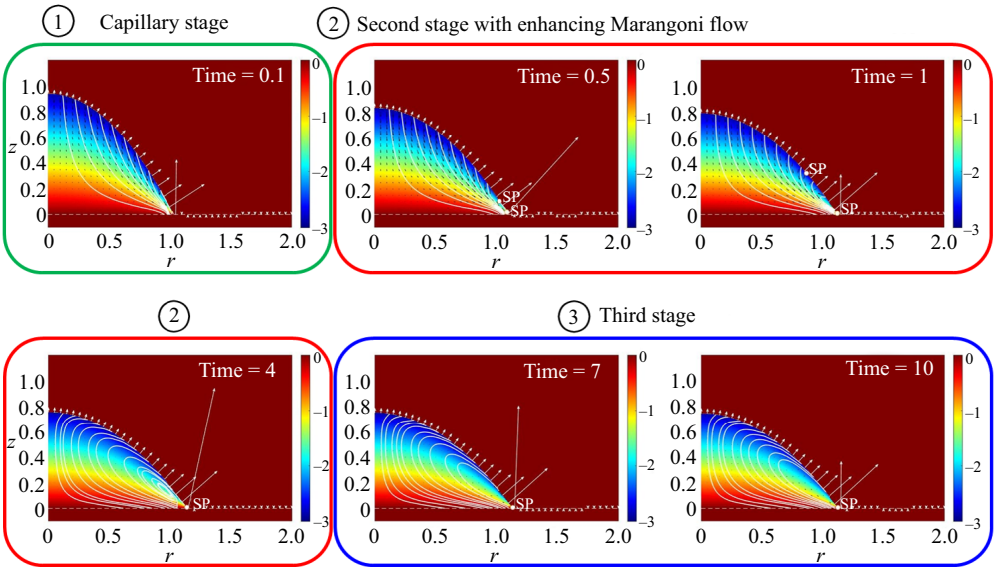

Figure 3. Evolution of flow state for an evaporative droplet on a thermal conductive substrate. The three stages are classified according to the state of internal flow, where continuous outwards capillary flow dominates droplet spreading at the initial stage, the Marangoni flow develops at the second stage and balances with the capillary flow at the third stage. The key dimensionless numbers in this case are set as $Ja^* = 5 \times 10^{-3}$, $Bi = 10^{-4}$ and $Ma = 10^{-2}$.

liquid phase, and the liquid–solid Biot number, Bi, which indicates the ratio of liquid phase to solid phase thermal resistance.

With decreasing Bi, heat dissipation into the substrate becomes efficient. In such cases, thermal resistance in the liquid phase dominates, thus the temperature gradient across the droplet surface is large from the droplet apex to the edge (large difference in thermal resistance across the liquid). The large temperature gradient strengthens the Marangoni flow and retards droplet spreading.

The Jakob number, mostly related to liquid volatility, decides the strength of evaporation cooling. For moderately volatile liquids, the evaporation mass flux takes heat away from the droplet surface, while the heat supply from the substrate is also considerable. Near the contact line, the liquid film is thin, enabling good heat supply and, thus, a higher temperature in comparison to the droplet apex; this is the case for many volatile liquids such as water and alcohol. At very high liquid volatility (small Ja, e.g. flash evaporation), heat supply from the substrate can no longer meet the heat loss from the droplet surface, as a result, the droplet surface gets 'uniformly cold', leading to weak thermal Marangoni flow. For liquids that hardly evaporate (low volatility and large Ja), the effect of evaporation cooling is negligible, and the process is near isothermal, which also leads to weak Marangoni effect.

Taking an overview of the dominating mechanisms, we can see that Ja (interfacial thermal effect) and Bi (heat conduction into the substrate) determine the temperature field in the droplet–solid system. Once the temperature gradient establishes, the Marangoni number, $Ma = \hat{\mu}_0 \hat{u}^*/\varepsilon\hat{\sigma}_0 = \hat{\eta}_\sigma \Delta\hat{T}/\hat{\sigma}_0$, determines the strength of the Marangoni flow. The Marangoni flow interacts with the capillary flow, which together affect the flow field inside the droplet, and further determine the droplet dynamics along with the nonuniform distribution of evaporation mass flux, as indicated by figure 4.

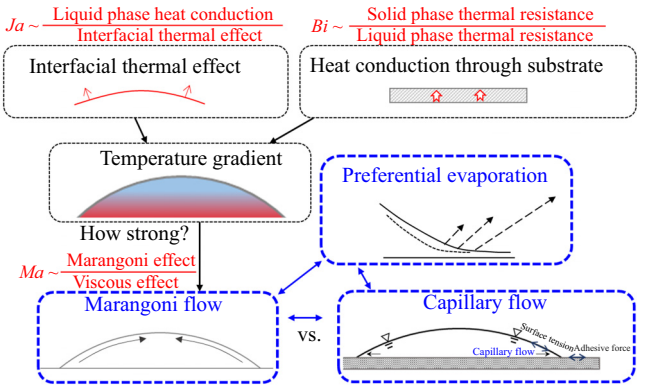

Figure 4. Decomposition of the dominating mechanisms in wetting dynamics of evaporative droplets.

4.2. *Limitations of the Hertz–Knudsen equation: appropriate scaling for comparison with experiments*

In the mathematical model, we formulate the expression of interfacial mass flux by combining the Hertz–Knudsen equation, the chemical potential difference across the liquid–air interface and the ideal gas assumption. The Hertz–Knudsen equation is often utilised to describe the evaporation and condensation rates based on the statistics of vapour molecules detaching from/adsorbing onto the liquid surface. Despite the correctness of the equation in describing the molecular motion across the interface, the derivation may deviate from experimental data that are tested at the macroscale. Specifically, the two empirical parameters (evaporation and condensation coefficients) contained in the equation have inexplicably been found to span three orders of magnitude (Young 1991; Fang & Ward 1999; Persad & Ward 2016). It is a common approach to adjust the values of these coefficients for a better fitting between experiments and simulations. Here, in order to facilitate a quantitative comparison with experiments, we follow a similar approach. Since the accommodation coefficients are incorporated into the Jakob number, we propose a systematic physics-based modification of Ja to account for the variation with the liquid/vapour properties and the environmental conditions.

Through systematic experiments on droplet evaporation and spreading, we found that this expression overpredicts the interfacial mass flux by 100–500 times (in comparison with the experimental values). In addition, the more volatile the liquid is, the more it overpredicts. The order of magnitude of overprediction corresponds with a number of work on water at 1 bar, e.g. Prüger (1940) and Delaney, Houston & Eagleton (1964) as summarised in figure 3 (evaporation coefficients), as well as Berman (1961) (film condensation) and Maa (1969) (direct condensation) as in figure 4 (condensation coefficients) in the work of Marek & Straub (2001). The variation trend of overprediction, i.e. more overprediction for more volatile liquids (weaker molecular bond at the interface), also corresponds with figure 7 in the work of Marek & Straub (2001) where weaker hydrogen bonds lead to smaller evaporation coefficients.

Based on the degree of overprediction and the trend, we propose the modification formula ($Ja^* = 500((\log_{max} - \log Ja)/(\log_{max} - \log_{min}))Ja$) for Jakob number Ja, where a unified correction is made for all test liquids with varying volatility. In the modification formula, we evaluate the liquid volatility by the order of magnitude of Ja (or, rather, saturation vapour pressure). Here $\log_{max}$ is the maximal order of magnitude of Ja and $\log_{min}$ is the minimal order of magnitude of Ja for liquids that are available in nature and

in normal fluid dynamics research, i.e. $\log_{max} = 0$, $\log_{min} = -4$ based on our calculations (note that there might be cases that exceed this range in extreme conditions, but we do not consider such cases which are rare in nature and the lab). With this general fitting, we correctly predict the evaporation mass flux for additional testing cases, e.g. by randomly setting the substrate temperature for a randomly selected liquids in our lab, which validates the proposed formula.

4.3. *Criterion of flow reversal*

To quantify the role of different effects on droplet dynamics, we decompose the dimensionless interfacial flow velocity u_s into thermal Marangoni velocity, u_{tg}, resulting from interfacial temperature gradient, and the capillary velocity, u_{ca}, related to the local surface curvature,

$$u_s = -\frac{h^2}{2\mu}\frac{\partial p}{\partial r} - \frac{h}{\mu}\frac{\partial T_s}{\partial r}, \quad u_{tg} = -\frac{h}{\mu}\frac{\partial T_s}{\partial r}, \quad u_{ca} = -\frac{h^2}{2\mu}\frac{\partial p}{\partial r}, \tag{4.1a–c}$$

where h is the location of liquid–gas interface, p is the pressure in the liquid phase and T_s is the interfacial temperature (liquid–gas), all from the numerical results.

Figure 5 maps the relative strength of thermal Marangoni flow and capillary flow in the short steady spreading stage, when the flow state becomes stable and the velocity ratio does not change much (stage ③ as in figure 3), $|u_{tg,max}|/|u_{ca,max}|$, for a wide range of combinations of Ja^* and Bi, along with decomposed interfacial velocity (figure 5*a–e*). With decreasing Bi from figure 5(*d*) to (*b*) to (*e*), the thermal Marangoni flow enhances and outweighs the capillary effect. As a result, the direction of interfacial flow reverses at a position close to the contact line, forming a SP as marked in figure 5(*b*,*e*).

From figure 5(*a*) to (*b*) to (*c*), the value of Ja^* increases, corresponding to decreasing liquid volatility. At a small value of Ja^*, severe liquid–vapour phase change takes place, preferentially at the contact line region, leading to the concentrated interplay of Marangoni and capillary effects near the contact line (figure 5*a*). The severe interfacial phase change also leads to uniformly cold droplet surface, corresponding to weak Marangoni effect. At large value of Ja^* (figure 5*c*), the whole process is close to isothermal due to weak evaporation. In such cases, the thermal Marangoni flow is also weak, and the droplet spreading is dominated by capillary flow, close to the case described by Tanner's law.

Overall, the thermal Marangoni effect becomes apparent and even outweighs the capillary effect at limited combinations of Ja^* and Bi. In regime II circled by dotted lines in figure 5, the thermal Marangoni effect is strong enough to reverse the flow direction and form a SP at the droplet surface. The droplet dynamics within this regime is therefore a joint result of the thermal Marangoni effect, evaporation effect and capillary effect, in contrast to the high-Ja^* regime where capillary effect dominates (regime I) and the low-Ja^* regime where liquid depletion due to evaporation near the contact line plays a significant role (regime III).

Previous studies, mostly experimentally, revealed the circulation reversal in evaporating droplets with varying substrate conductivity. We recalculated the experimental data in these pioneer work (Ristenpart *et al.* 2007; Xu *et al.* 2010), which are demonstrated in the phase diagram and show good correspondence with our theoretical predictions. Due to technical limitations, liquids in those studies are limited to water and alcohols where the evaporation is moderate with sufficient time for observation, and the substrates are mostly glass for microPIV visualisation. With the criterion proposed in figure 5, we are able to quickly find out the flow state for liquids with varying thermal conductivity and volatility,

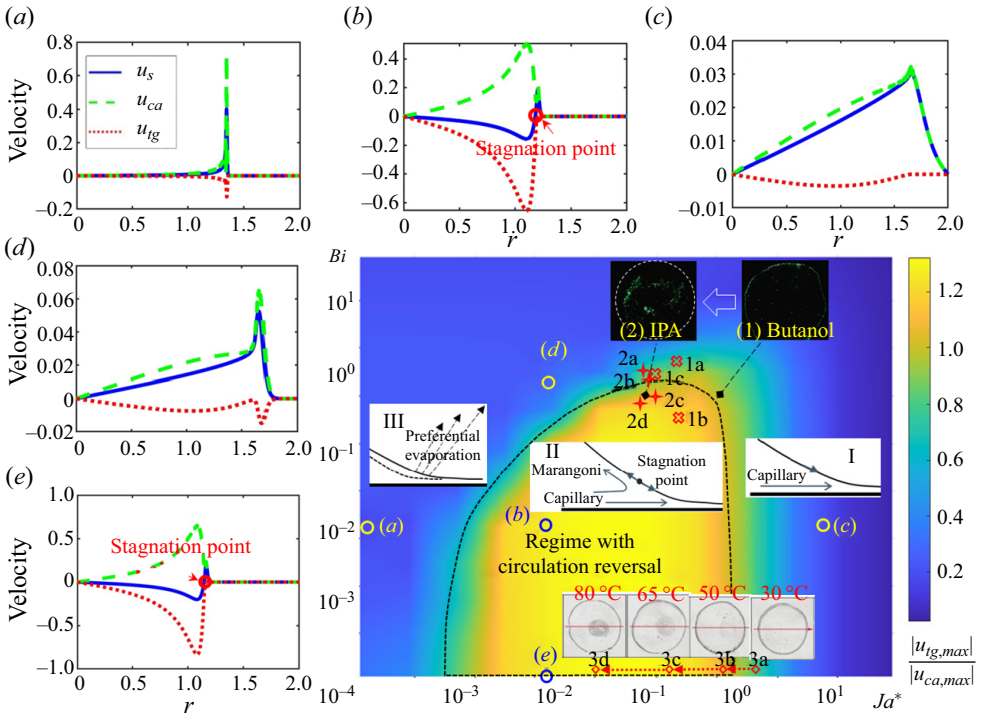

Figure 5. Phase diagram for the relative strength of thermal Marangoni flow to capillary flow. (*a–e*) Decomposition of surface velocity u_s to thermal Marangoni velocity u_{tg} and capillary velocity u_{ca}, corresponding to letters (*a–e*) in the colourmap. Sketches I, II and III indicate the dominating mechanism at different regimes of the phase diagram. The experimental data by Xu *et al.* (2010) (1a, water on glass of thickness 1 mm; 1b, water on glass of thickness 0.15 mm; 1c, IPA on glass of thickness 1 mm), Ristenpart *et al.* (2007) (2 µl droplets of: 2a, methanol; 2b, ethanol; 2c, IPA; 2d, chloroform; on PDMS of thickness 4 mm) and Li *et al.* (2015) (3a to 3b with leftward dotted arrows and representative deposition patterns: 2.5 µl droplets on glass substrate of 30, 50, 65 and 80 °C) are marked out, which indicate the flow reversal inside the droplet with changing environmental settings. Note that the dotted line presents the criterion for the formation of SP, and does not necessarily correspond to the contour line of $|u_{tg,max}|/|u_{ca,max}| = 1$.

and on substrates with varying thickness and thermal properties, which could not have been possible solely based on experimental observations.

We additionally visualised the flow field near the bottom of droplets with different volatility (Supplementary movie 3). For less-volatile butanol, continuous outward flow is observed driven by the capillary force, which forms a ‘coffee ring’ as the droplet dries out (figure 6*a*). As the liquid volatility increases (IPA), the PIV particles tend to change its direction at a position near the three-phase contact line (SP), where a turning point in the tracing track of fluorescent particles is observed as in figure 6(*b*). The direction change avoids particle accumulation at the periphery, which leads to more uniform deposition patterns as the droplet fully dries out. The transition of flow direction and the formation of deposition patterns correspond with our numerical predictions by locating the Ja^*–Bi coordinates for (1) butanol–1.1 mm slide glass and (2) IPA–1.1 mm slide glass in figure 5. In correspondence to the flow direction, the deposition transits from coffee ring to more uniform patterns as indicated by the deposited fluorescent tracing particles from (1) butanol and (2) IPA droplets in figure 5.

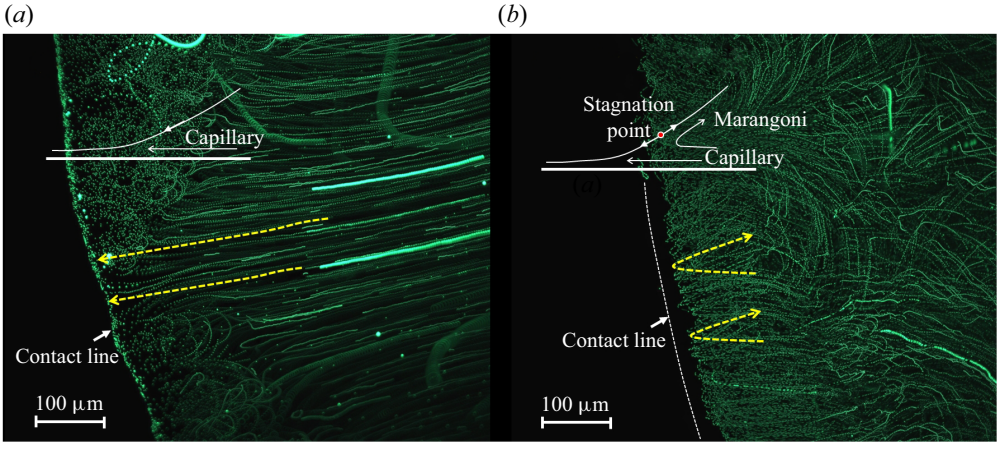

Figure 6. Flow pattern near three phase contact line visualised by tracer particles where the tracing tracks of fluorescent particles are overlap of 100 continuous frames: (*a*) a 0.5 μl butanol droplet on slide glass and (*b*) a 0.5 μl IPA droplet on slide glass.

In addition to the experiments in present work, the proposed phase diagram also correctly predicts the transition of deposition patterns from coffee ring (Deegan *et al.* 1997) to coffee eye with substrate heating (Li *et al.* 2015), where the saturation vapour pressure increases and evaporation enhances with increasing substrate temperature, corresponding to decreasing Ja^* as indicated by diamond marks 3a to 3d along with leftward dotted arrows in figure 5. The phase diagram thus provides an efficient approach for quick prediction and control of deposition patterns in applications including printing, coating and thin film fabrication.

4.4. *Spreading law of volatile droplets*

The interfacial phase change and interacting flows further decide the spreading dynamics of the droplet. Specifically, the speed of contact line can be quantified with a power law in the form of $R(t) = t^n$, where n is the spreading exponent. We then check the flow state and evaluate the corresponding spreading rate for a wide range of Ja^* and Bi. A phase diagram is thereafter derived with representative cases shown in figure 7.

Overall, the spreading exponent decreases from 1/10 (Tanner's law) to smaller values $(1/11, 1/12, \ldots, 1/25)$ with decreasing Ja^* and decreasing Bi. As Bi decreases, heat transport across the substrate gets efficient and the thermal resistance in the liquid phase becomes dominant. This strengthens both the evaporation mass flux and the thermal Marangoni flow (enlarged temperature gradient), both of which retard droplet spreading.

With decreasing Ja^*, the evaporation effect enhances, whereas the thermal Marangoni flow strengthens first (from isothermal state to large temperature gradient) and then weakens (as the droplet surface uniformly cools due to the strong evaporation cooling effect). The joint effect of non-uniform evaporation and thermal Marangoni flow shows in the slow down of droplet spreading with decreasing Ja^*. In addition, the influence of substrate thermal properties on the spreading rate is weak at small liquid volatility and becomes significant at high liquid volatility as the evaporation cooling effect strengthens and the efficiency of heat supply becomes eminent.

To validate our theoretical findings, a series of experiments were conducted with selected liquids and solid substrates. To ensure uniform spreading and minimise hysteresis,

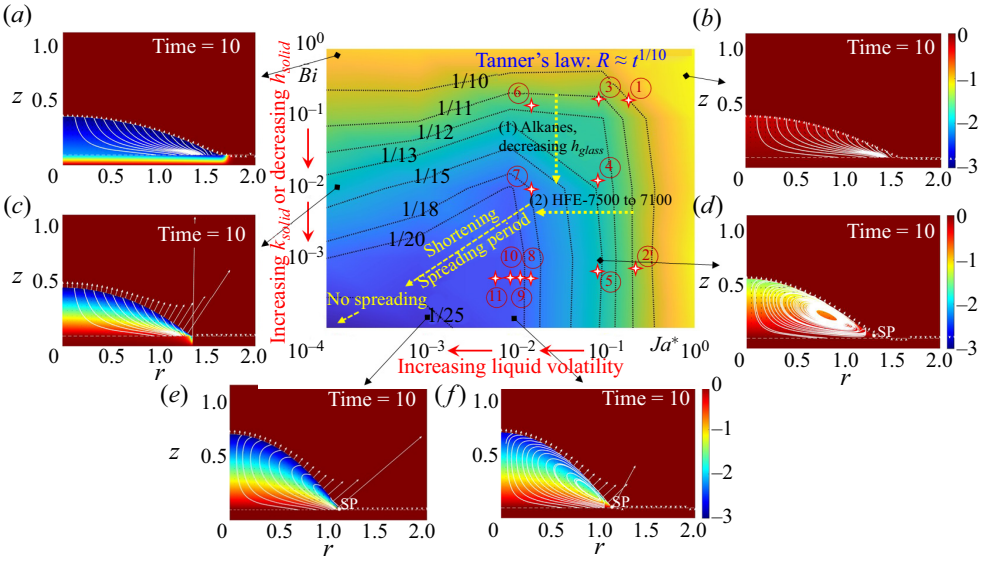

Figure 7. Phase diagram for the spreading rate of droplets along with demonstrations of flow and temperature fields in representative conditions. Contour lines of the spreading exponent are marked out with corresponding values. Experimental results by Shiri *et al.* (2021) ((1) alkanes on glass substrates with decreasing thickness) and Kumar *et al.* (2022) ((2) HFE 7500 to 7100 with increasing volatility) are presented with yellow dotted arrows. Experimental results in our research are marked with stars numbered as ① butanol on 1.1 mm glass, ② butanol on 1.0 mm copper, ③ IPA on 1.1 mm glass, ④ IPA on 1.0 mm SUS430, ⑤ IPA on 1.0 mm copper, ⑥ FC-72 on 1.1 mm glass, ⑦ FC-72 on 1.0 mm SUS430, ⑧ FC-72 on 1.0 mm copper (①–⑧ are cases with substrate temperature $T_{sub} = 20\,^{\circ}\mathrm{C}$), ⑨ FC-72 on 1.0 mm copper ($T_{sub} = 25\,^{\circ}\mathrm{C}$), ⑩ FC-72 on 1.0 mm copper ($T_{sub} = 35\,^{\circ}\mathrm{C}$) and ⑪ FC-72 on 1.0 mm copper ($T_{sub} = 45\,^{\circ}\mathrm{C}$).

we prepared substrates with mirror finishing with the downward-side substrate temperature controlled as $20 \pm 0.2\,^{\circ}\mathrm{C}$. Experiments were conducted with 1-butanol ($p_{sat,20\,^{\circ}\mathrm{C}} = 580$ Pa), 2-propanol (IPA, $p_{sat,20\,^{\circ}\mathrm{C}} = 4420$ Pa) and FluorinertR (FC-72, $p_{sat,25\,^{\circ}\mathrm{C}} = 30\,900$ Pa), each with one order of magnitude higher saturation vapour pressure, and on different substrates, i.e. glass ($k_{glass} = 0.8$ W m^{-1} K^{-1}, $h_{glass} = 1.1$ mm), SUS430 ($k_{SUS430} = 25$ W m^{-1} K^{-1}, $h_{SUS430} = 1.0$ mm), copper ($k_{copper} = 398$ W m^{-1} K^{-1}, $h_{copper} = 1.0$ mm), each with one order of magnitude higher thermal conductivity. We also tried to further enhance the evaporation effect by increasing the downward side temperature of the substrate to 25 °C, 35 °C and 45 °C. The calculated values of Ja^* and Bi for cases ① to ⑪ are summarised in table 3, which correspond with the data points marked in the phase diagram in figure 7.

In the experiments, the droplet is deposited onto the substrate right after its generation from the syringe, however close the distance between the droplet and the substrate is, it unavoidably has inertia (non-zero initial velocity) that pushes the contact line forwards. This stage when inertia effect dominates exhibits higher spreading rate, e.g. $R \sim t^{\alpha}$, $\alpha = 1/4 \sim 1/2$, typically between 0.1 and 10 ms (Ding & Spelt 2007; Bird *et al.* 2008; Chen *et al.* 2013). As the droplet relaxes, viscous dissipation within the droplet becomes the main source resisting spreading, and the spreading radius follows Tanner's law, $r \sim t^{1/10}$, for non-volatile liquids (Tanner 1979). In the proposed research, we focus on the 'Tanner's regime' (or inertia-free regime) and investigate the influence of substrate conductivity and

https://doi.org/10.1017/jfm.2024.385 Published online by Cambridge University Press

Case	①	②	③	④	⑤	⑥	⑦	⑧	⑨	⑩	⑪
Bi	2.8×10^{-1}	8.1×10^{-4}	2.5×10^{-1}	1.1×10^{-2}	7.0×10^{-4}	1.7×10^{-1}	7.6×10^{-3}	4.9×10^{-4}	4.9×10^{-4}	4.9×10^{-4}	4.9×10^{-4}
Ja^*	7.0×10^{-1}	7.0×10^{-1}	1.1×10^{-1}	1.1×10^{-1}	1.1×10^{-1}	1.9×10^{-2}	1.9×10^{-2}	1.9×10^{-2}	1.6×10^{-2}	1.1×10^{-2}	7.9×10^{-3}

Table 3. Values of Ja^* and Bi for cases ① to ⑪ (expressed in scientific notation).

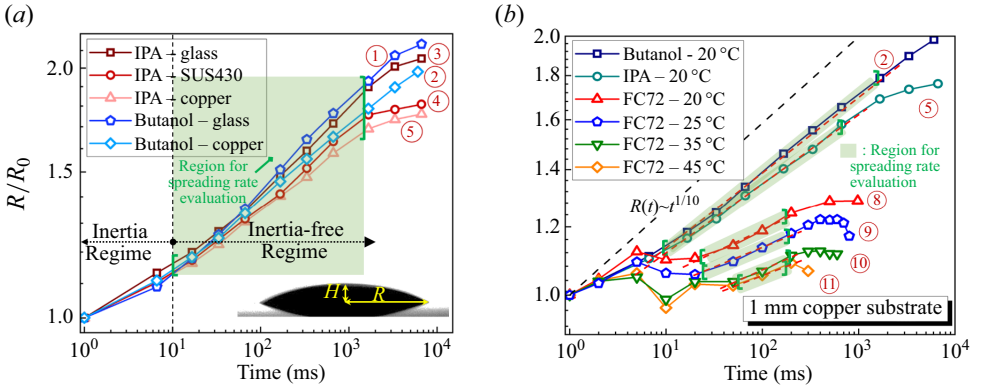

Figure 8. (*a*) Spreading behaviours of droplets at substrates with different thermal conductivity (T_{sub} = 20 °C): ① IPA on 1.1 mm glass, ② IPA on 1.0 mm SUS430, ③ IPA on 1.0 mm copper, ④ butanol on 1.1 mm glass, ⑤ butanol on 1 mm copper. (*b*) Spreading behaviours of droplets with different volatility on 1.0 mm copper substrate: ② butanol at T_{sub} = 20 °C, ⑤ IPA at T_{sub} = 20 °C, ⑧–⑪ FC-72 at T_{sub} = 20 °C, 25 °C, 35 °C, 45 °C. These cases correspond with the mark numbers in figure 7.

liquid volatility on this stage of spreading. This requires us to do linear fitting to log–log plot for droplet spreading after 10 ms from its deposition (green regions as in figure 8).

Figure 8(*a*) compares the spreading rate of droplets at different substrate conductivity. By changing the substrate material from glass to SUS430 and to copper, the slope of the variation curve decreases, indicating a decreasing trend of spreading rate with increasing substrate conductivity (① → ②, ③ → ④ → ⑤).

The effect of liquid volatility on the spreading dynamics of the droplet is stronger than that of the substrate conductivity, as indicated by figure 8(*b*). For FC-72 droplets, a slight fluctuation (spread and contract) takes place at the very initial moment (< 10 ms) as a result of inertia effect (the inertia effect can cause a slight fluctuation as the surface tension of FC-72 is small, even though the distance for deposition is controlled to be as small as possible). The droplet then spreads, slows down and recedes after several hundred milliseconds. Here we focus on the short spreading period marked as green regions in figure 8(*b*).

With increasing liquid volatility, we can see an apparent decrease in the spreading rate (② Butanol → ⑤ IPA → ⑧ FC-72 in figure 8*b*). By further increasing the substrate temperature, the spreading rate further decreases and the period of spreading shortens as indicated by ⑧ 20 °C → ⑨ 25 °C → ⑩ 35 °C → ⑪ 45 °C in figure 8(*b*). For substrate temperature higher than 45 °C ($T_{FC\text{-}72,boiling}$ = 56 °C), the spreading stage is no longer distinguishable and no apparent spreading can be observed, i.e. the contact line recedes right after the droplet deposition due to significant mass loss at the contact line region, representing a general scenario in flash evaporation.

We further apply the calculated dimensionless numbers to the proposed model, and get the spreading component at the steady spreading stage. Very nice quantitative correspondence is found between experimental and theoretical values as summarised in table 4. Here, the experimental liquids and substrates cover most of the cases that span from non-volatile to the most-volatile liquids in practical applications and on substrates with a full range of thermal conductivity, thus allowing for reliable prediction of the liquid behaviours by quickly locating its Ja^*–Bi coordinate in the phase diagram.

Besides the experiments in present research, our conclusions on the effect of substrate thermal properties correspond with the work of Shiri *et al.* (2021) where alkane droplets

No.	Exp.	Num.	No.	Exp.	Num.	No.	Exp.	Num.
①	0.0995 ± 0.0028	0.103	②	0.092 ± 0.0028	0.0936	③	0.0894 ± 0.0026	0.0910
④	0.0869 ± 0.0026	0.0813	⑤	0.0803 ± 0.0053	0.0788	⑥	0.0634 ± 0.0024	0.0752
⑦	0.0601 ± 0.0011	0.0578	⑧	0.0568 ± 0.0052	0.0504	⑨	0.0481 ± 0.0036	0.0490
⑩	0.0473 ± 0.0030	0.0446	⑪	0.0429 ± 0.0010	0.0435	—	—	—

Table 4. Experimental (Exp.) spreading exponent n in comparison with the numerical (Num.) value by matching its position (Ja^*, Bi) in the phase diagram. Numbers ①–⑪ correspond with the cases marked in figure 7. Deviations between experimental and numerical results exist mainly in the high-volatility and low-substrate-conductivity region (small Ja^* and large Bi, e.g. case ⑥), where the heat dissipation into the gas phase is no longer negligible.

indicate increasing contact angle and slowing-down spreading rate as the thickness of the glass substrate decreases stepwise from 6 mm to 0.063 mm. The influence of liquid volatility also meets with a very recent work by Kumar *et al.* (2022) where the spreading rate of HFE-7500 to HFE-7100 droplets decreases with increasing liquid volatility (decreasing chain length). These uniform findings allow for optimal design of working fluids and substrates in phase change thermal management and dry-out prevention for high-power-density electronics, which requires a balance between liquid wetting and thermal efficiency.

5. Conclusions and perspectives

In this research, we have revisited the classical problem of droplet wetting with interfacial phase change, which is of fundamental importance to a wide range of industrial processes that involve three phases. The objective originates from the urgent need for a unified explanation to a couple of basic scientific problems including the flow transition for different liquid–solid combinations, the existence of SP near the three phase contact line, the relative strength of capillary and Marangoni flows, the deposition patterns from colloidal suspensions, as well as the corresponding spreading dynamics in diverse scenarios. Due to the requirement for substrate transparency and the available frame rate of existing visualisation techniques, explorations on these scientific issues are limited to substrates such as glass, and common liquids such as water and alcohol, whereas important liquids and substrates in the vast industrial fields are less explored, such as refrigerants and metallic substrates. This requires a close collaboration between experimental and numerical efforts, where information that cannot be revealed from one side can be disclosed by the other.

Here, we have developed a lubrication-type model that considers the non-isothermal heat conduction into the solid substrate. We have further conducted experiments on the flow field and the spreading rate for a wide range of combinations of liquids and solids. With one-to-one comparison between the numerical and experimental results, we have elucidated the key dimensionless numbers that come into effect, i.e. the Jakob number, Ja, the liquid–solid Biot number, Bi, and the Marangoni number, Ma. Unified criteria have been proposed for the transition of flow state, and we have provided unbiased explanations to a series of individual works on deposition patterns from drying droplets. A phase diagram for spreading dynamics has further been established along with experimental demonstrations, which extend Tanner's law (for non-volatile liquids in an isotherm state) to a full range of liquids with saturation vapour pressure spanning from 10^1 to 10^4 Pa

and on substrates with the entire range of thermal conductivity spanning from 10^{-1} to 10^{3} W m^{-1} K^{-1}.

In the theoretical aspect, this work has illustrated the relative strength of interacting physical mechanisms as regimes I, II and III in figure 5, where the capillary effect dominates at low liquid volatility in regime I, the Marangoni effect, capillary effect and evaporation effect interact in regime II and the strong evaporation effect (preferential mass loss near contact line) dominates in regime III at very high liquid volatility. Such decomposition of the mechanisms allows for quick positioning of the influencing factors, and enables efficient control of liquid behaviours in various phase change energy devices, printing–coating processes and microfluidic systems.

Overall, Tanner's law describes the spreading of non-volatile Newtonian fluids on smooth solid substrates. Here 'non-volatile', 'Newtonian' and 'smooth' are necessary conditions for the universality of the spreading exponent. With interfacial phase change (volatile liquids), the process becomes non-isothermal in which case the non-uniform distribution of mass flux and the thermal Marangoni effect come into play along with the capillary and viscous effect, as quantified in the present work. For non-Newtonian fluids, the viscosity largely depends on the shear stress. Theories for the spreading dynamics of dilatant fluids (shear thickening) and pseudo-plastic fluids (shear thinning) were established in previous studies based on the lubrication approximation (Rafaï *et al.* 2004; Wang *et al.* 2007*a*) and experiments (Wang *et al.* 2007*b*), and the explorations are still ongoing. For topological surfaces with microstructures, the spreading dynamics can be more complex. A systematic understanding is yet reached due to the diverse surface topology and the complex liquid–solid interaction, where the small-scale surface structure affects the dynamics of the contact line and thereafter the overall droplet behaviours. By taking advantage of the asymmetric effect of surface topology, it is also possible to realise directional fluid motion, which indeed has been widely exploited in recent years with promising applications in directional liquid transport (Li *et al.* 2017; Li, Li & Dong 2020), water harvesting (Zheng *et al.* 2010; Dai *et al.* 2018) and dry-out prevention (Li *et al.* 2021).

Supplementary movies. Supplementary movies are available at https://doi.org/10.1017/jfm.2024.385.

Funding. The authors gratefully acknowledge the support received from Japanese Society for the Promotion of Science (JSPS), and ThermaSMART project of European Commission (grant no. EC-H2020-RISE-ThermaSMART-778104). Z.W. and C.I. acknowledge the support from JSPS KAKENHI (grant nos JP21K14097, JP21H01251, JP22K18771, JP24K17218).

Declaration of interests. The authors report no conflict of interest.

Author ORCIDs.
Zhenying Wang https://orcid.org/0000-0002-2651-1808;
George Karapetsas https://orcid.org/0000-0002-3486-7484;
Prashant Valluri https://orcid.org/0000-0003-4917-8283;
Chihiro Inoue https://orcid.org/0000-0002-8191-9275.

References

Ajaev, V.S. 2005 Spreading of thin volatile liquid droplets on uniformly heated surfaces. *J. Fluid Mech.* **528**, 279–296.

Anderson, D.M. & Davis, S.H. 1995 The spreading of volatile liquid droplets on heated surfaces. *Phys. Fluids* **7** (2), 248–265.

Atkins, P., Atkins, P.W. & de Paula, J. 2014 *Atkins' Physical Chemistry*. Oxford University Press.

BERMAN, L.D. 1961 Soprotivlenie na granize razdela fas pri plenochnoi kondensazii para nizkogo davleniya. *Tr. Vses. Ni, i Konstrukt In-t Khim. Mashinost* **36**, 66.

BERTELOOT, G., PHAM, C.-T., DAERR, A., LEQUEUX, F. & LIMAT, L. 2008 Evaporation-induced flow near a contact line: consequences on coating and contact angle. *Europhys. Lett.* **83** (1), 14003.

BIRD, J.C., MANDRE, S. & STONE, H.A. 2008 Short-time dynamics of partial wetting. *Phys. Rev. Lett.* **100** (23), 234501.

BLAKE, T.D. 2006 The physics of moving wetting lines. *J. Colloid Interface Sci.* **299** (1), 1–13.

BONN, D., EGGERS, J., INDEKEU, J., MEUNIER, J. & ROLLEY, E. 2009 Wetting and spreading. *Rev. Mod. Phys.* **81** (2), 739.

BREITENBACH, J., ROISMAN, I.V. & TROPEA, C. 2018 From drop impact physics to spray cooling models: a critical review. *Exp. Fluids* **59**, 1–21.

CARLSON, A. 2018 Fluctuation assisted spreading of a fluid filled elastic blister. *J. Fluid Mech.* **846**, 1076–1087.

CARRÉ, A., GASTEL, J.-C. & SHANAHAN, M.E.R. 1996 Viscoelastic effects in the spreading of liquids. *Nature* **379** (6564), 432–434.

CAZABAT, A.M. & STUART, M.A.C. 1986 Dynamics of wetting: effects of surface roughness. *J. Phys. Chem.* **90** (22), 5845–5849.

CHARITATOS, V. & KUMAR, S. 2020 A thin-film model for droplet spreading on soft solid substrates. *Soft Matt.* **16** (35), 8284–8298.

CHEN, K.-T., LI, Q.-Y., OMORI, T., YAMAGUCHI, Y., IKUTA, T. & TAKAHASHI, K. 2022 Slip length measurement in rectangular graphene nanochannels with a 3D flow analysis. *Carbon* **189**, 162–172.

CHEN, L., BONACCURSO, E. & SHANAHAN, M.E.R. 2013 Inertial to viscoelastic transition in early drop spreading on soft surfaces. *Langmuir* **29** (6), 1893–1898.

CHENG, K., LI, Q.-Y., WANG, Z., FUKUNAGA, T., TESHIMA, H. & TAKAHASHI, K. 2024 Temperature-dependent water slip flow combined with capillary evaporation in graphene nanochannels. *Intl J. Heat Mass Transfer* **225**, 125451.

CORMIER, S.L., MCGRAW, J.D., SALEZ, T., RAPHAËL, E. & DALNOKI-VERESS, K. 2012 Beyond Tanner's law: crossover between spreading regimes of a viscous droplet on an identical film. *Phys. Rev. Lett.* **109** (15), 154501.

DAI, Q., KHONSARI, M.M., SHEN, C., HUANG, W. & WANG, X. 2016 Thermocapillary migration of liquid droplets induced by a unidirectional thermal gradient. *Langmuir* **32** (30), 7485–7492.

DAI, X., SUN, N., NIELSEN, S.O., STOGIN, B.B., WANG, J., YANG, S. & WONG, T.-S. 2018 Hydrophilic directional slippery rough surfaces for water harvesting. *Sci. Adv.* **4** (3), eaaq0919.

DE GENNES, P.-G. 1985 Wetting: statics and dynamics. *Rev. Mod. Phys.* **57** (3), 827.

DE GENNES, P.G., HUA, X. & LEVINSON, P. 1990 Dynamics of wetting: local contact angles. *J. Fluid Mech.* **212**, 55–63.

DEEGAN, R.D., BAKAJIN, O., DUPONT, T.F., HUBER, G., NAGEL, S.R. & WITTEN, T.A. 1997 Capillary flow as the cause of ring stains from dried liquid drops. *Nature* **389** (6653), 827–829.

DELANEY, L.J., HOUSTON, R.W. & EAGLETON, L.C. 1964 The rate of vaporization of water and ice. *Chem. Engng Sci.* **19** (2), 105–114.

DING, H. & SPELT, P.D.M. 2007 Inertial effects in droplet spreading: a comparison between diffuse-interface and level-set simulations. *J. Fluid Mech.* **576**, 287–296.

DUNN, G.J., WILSON, S.K., DUFFY, B.R., DAVID, S. & SEFIANE, K. 2009 The strong influence of substrate conductivity on droplet evaporation. *J. Fluid Mech.* **623**, 329–351.

FANG, G. & WARD, C.A. 1999 Temperature measured close to the interface of an evaporating liquid. *Phys. Rev.* E **59** (1), 417.

GOOSSENS, S., SEVENO, D., RIOBOO, R., VAILLANT, A., CONTI, J. & DE CONINCK, J. 2011 Can we predict the spreading of a two-liquid system from the spreading of the corresponding liquid–air systems? *Langmuir* **27** (16), 9866–9872.

HOANG, A. & KAVEHPOUR, H.P. 2011 Dynamics of nanoscale precursor film near a moving contact line of spreading drops. *Phys. Rev. Lett.* **106** (25), 254501.

HU, H. & LARSON, R.G. 2005 Analysis of the effects of Marangoni stresses on the microflow in an evaporating sessile droplet. *Langmuir* **21** (9), 3972–3980.

HU, H. & LARSON, R.G. 2006 Marangoni effect reverses coffee-ring depositions. *J. Phys. Chem.* B **110** (14), 7090–7094.

JALAAL, M., STOEBER, B. & BALMFORTH, N.J. 2021 Spreading of viscoplastic droplets. *J. Fluid Mech.* **914**, A21.

JAMBON-PUILLET, E., CARRIER, O., SHAHIDZADEH, N., BRUTIN, D., EGGERS, J. & BONN, D. 2018 Spreading dynamics and contact angle of completely wetting volatile drops. *J. Fluid Mech.* **844**, 817–830.

KARAPETSAS, G., SAHU, K.C. & MATAR, O.K. 2013 Effect of contact line dynamics on the thermocapillary motion of a droplet on an inclined plate. *Langmuir* **29** (28), 8892–8906.

KAVEHPOUR, H.P., OVRYN, B. & MCKINLEY, G.H. 2003 Microscopic and macroscopic structure of the precursor layer in spreading viscous drops. *Phys. Rev. Lett.* **91** (19), 196104.

KUMAR, M., PARIMALANATHAN, S., REDNIKOV, A. & COLINET, P. 2022 Wetting dynamics of volatile hydrofluoroether (HFE) liquid droplets. *Bull. Am. Phys. Soc.* **67**, 19.

LELAH, M.D. & MARMUR, A. 1981 Spreading kinetics of drops on glass. *J. Colloid Interface Sci.* **82** (2), 518–525.

LI, J., ZHOU, X., LI, J., CHE, L., YAO, J., MCHALE, G., CHAUDHURY, M.K. & WANG, Z. 2017 Topological liquid diode. *Sci. Adv.* **3** (10), eaao3530.

LI, J., ZHOU, X., TAO, R., ZHENG, H. & WANG, Z. 2021 Directional liquid transport from the cold region to the hot region on a topological surface. *Langmuir* **37** (16), 5059–5065.

LI, X., LI, J. & DONG, G. 2020 Bioinspired topological surface for directional oil lubrication. *ACS Appl. Mater. Interfaces* **12** (4), 5113–5119.

LI, Y., LV, C., LI, Z., QUÉRÉ, D. & ZHENG, Q. 2015 From coffee rings to coffee eyes. *Soft Matt.* **11** (23), 4669–4673.

MAA, J.R. 1969 Condensation studies with jet stream tensimeter. *Ind. Engng Chem. Fundam.* **8** (3), 564–570.

MAREK, R. & STRAUB, J. 2001 Analysis of the evaporation coefficient and the condensation coefficient of water. *Intl J. Heat Mass Transfer* **44** (1), 39–53.

MARMUR, A. 1983 Equilibrium and spreading of liquids on solid surfaces. *Adv. Colloid Interface Sci.* **19** (1–2), 75–102.

MITRA, S. & MITRA, S.K. 2016 Understanding the early regime of drop spreading. *Langmuir* **32** (35), 8843–8848.

MOOSMAN, S. & HOMSY, G.M. 1980 Evaporating menisci of wetting fluids. *J. Colloid Interface Sci.* **73** (1), 212–223.

MUDAWAR, I. 2001 Assessment of high-heat-flux thermal management schemes. *IEEE Trans. Compon. Packag. Technol.* **24** (2), 122–141.

PANG, K.E. & NÁRAIGH, L.Ó. 2022 A mathematical model and mesh-free numerical method for contact-line motion in lubrication theory. *Environ. Fluid Mech.* **22** (2–3), 301–336.

PERSAD, A.H. & WARD, C.A. 2016 Expressions for the evaporation and condensation coefficients in the Hertz–Knudsen relation. *Chem. Rev.* **116** (14), 7727–7767.

PLESSET, M.S. & PROSPERETTI, A. 1976 Flow of vapour in a liquid enclosure. *J. Fluid Mech.* **78** (3), 433–444.

PRÜGER, W. 1940 Die verdampfungsgeschwindigkeit der flüssigkeiten. *Z. Phys.* **115** (3–4), 202–244.

RAFAÏ, S., BONN, D. & BOUDAOUD, A. 2004 Spreading of non-Newtonian fluids on hydrophilic surfaces. *J. Fluid Mech.* **513**, 77–85.

RISTENPART, W.D., KIM, P.G., DOMINGUES, C., WAN, J. & STONE, H.A. 2007 Influence of substrate conductivity on circulation reversal in evaporating drops. *Phys. Rev. Lett.* **99** (23), 234502.

ROSE, J.W. 2002 Dropwise condensation theory and experiment: a review. *Proc. Inst. Mech. Engs* A **216** (2), 115–128.

SAISEAU, R., PEDERSEN, C., BENJANA, A., CARLSON, A., DELABRE, U., SALEZ, T. & DELVILLE, J.-P. 2022 Near-critical spreading of droplets. *Nat. Commun.* **13** (1), 7442.

SCHNEIDER, C.A., RASBAND, W.S. & ELICEIRI, K.W. 2012 NIH Image to ImageJ: 25 years of image analysis. *Nat. Meth.* **9** (7), 671–675.

SHIRI, S., SINHA, S., BAUMGARTNER, D.A. & CIRA, N.J. 2021 Thermal Marangoni flow impacts the shape of single component volatile droplets on thin, completely wetting substrates. *Phys. Rev. Lett.* **127** (2), 024502.

TANNER, L.H. 1979 The spreading of silicone oil drops on horizontal surfaces. *J. Phys.* D*: Appl. Phys.* **12** (9), 1473.

TEH, S.-Y., LIN, R., HUNG, L.-H. & LEE, A.P. 2008 Droplet microfluidics. *Lab on a Chip* **8** (2), 198–220.

TSOUMPAS, Y., DEHAECK, S., REDNIKOV, A. & COLINET, P. 2015 Effect of Marangoni flows on the shape of thin sessile droplets evaporating into air. *Langmuir* **31** (49), 13334–13340.

TU, Y., WANG, R., ZHANG, Y. & WANG, J. 2018 Progress and expectation of atmospheric water harvesting. *Joule* **2** (8), 1452–1475.

VOINOV, O.V. 1976 Hydrodynamics of wetting. *Fluid Dyn.* **11** (5), 714–721.

WANG, L. & HARRIS, M.T. 2018 Stagnation point of surface flow during drop evaporation. *Langmuir* **34** (20), 5918–5925.

WANG, X.D., LEE, D.J., PENG, X.F. & LAI, J.Y. 2007*a* Spreading dynamics and dynamic contact angle of non-Newtonian fluids. *Langmuir* **23** (15), 8042–8047.

WANG, X.D., ZHANG, Y., LEE, D.J. & PENG, X.F. 2007*b* Spreading of completely wetting or partially wetting power-law fluid on solid surface. *Langmuir* **23** (18), 9258–9262.

WANG, Z., KARAPETSAS, G., VALLURI, P. & INOUE, C. 2024 Flow structure near three phase contact line of low-contact-angle evaporating droplets. *Appl. Phys. Lett.* **124**, 101603.

WANG, Z., KARAPETSAS, G., VALLURI, P., SEFIANE, K., WILLIAMS, A. & TAKATA, Y. 2021 Dynamics of hygroscopic aqueous solution droplets undergoing evaporation or vapour absorption. *J. Fluid Mech.* **912**, A2.

WANG, Z., OREJON, D., SEFIANE, K. & TAKATA, Y. 2019 Coupled thermal transport and mass diffusion during vapor absorption into hygroscopic liquid desiccant droplets. *Intl J. Heat Mass Transfer* **134**, 1014–1023.

WANG, Z., OREJON, D., SEFIANE, K. & TAKATA, Y. 2020 Effect of substrate conductivity on the transient thermal transport of hygroscopic droplets during vapor absorption. *Micromachines* **11** (2), 193.

WANG, Z., OREJON, D., TAKATA, Y. & SEFIANE, K. 2022 Wetting and evaporation of multicomponent droplets. *Phys. Rep.* **960**, 1–37.

WANG, Z., ZHANG, X. & LI, Z. 2017 Investigation on the coupled heat and mass transfer process between extremely high humidity air and liquid desiccant in the counter-flow adiabatic packed tower. *Intl J. Heat Mass Transfer* **110**, 898–907.

XU, X. & LUO, J. 2007 Marangoni flow in an evaporating water droplet. *Appl. Phys. Lett.* **91** (12), 124102.

XU, X., LUO, J. & GUO, D. 2010 Criterion for reversal of thermal Marangoni flow in drying drops. *Langmuir* **26** (3), 1918–1922.

YANG, X., WU, M.M., DOI, M. & MAN, X. 2022 Evaporation dynamics of sessile droplets: the intricate coupling of capillary, evaporation, and Marangoni flow. *Langmuir* **38** (16), 4887–4893.

YOUNG, J.B. 1991 The condensation and evaporation of liquid droplets in a pure vapour at arbitrary Knudsen number. *Intl J. Heat Mass Transfer* **34** (7), 1649–1661.

ZHENG, Y., BAI, H., HUANG, Z., TIAN, X., NIE, F.-Q., ZHAO, Y., ZHAI, J. & JIANG, L. 2010 Directional water collection on wetted spider silk. *Nature* **463** (7281), 640–643.